**ORIGINAL PAPER**

# A study of rock mass properties based on discrete fracture network modeling and compression damage process

Ming Li[1] · Hui Deng[1] · Guoxing Tu[1]

## Abstract

Rock masses are inherently complex media, composed of intact rocks and fractures, and their mechanical behavior and deformation characteristics are significantly influenced by the characteristics and development of fractures. In this study, a discrete fracture network (DFN) model was constructed based on comprehensive field surveys and meticulous laboratory tests. By utilizing the finite-discrete element method (FDEM), we conducted simulated compression tests on the rock mass in the cavern area of the GS hydropower station. The expansion patterns and stress–strain characteristics of fractures during compression were meticulously analyzed, allowing the rock mass failure process to be categorized into four distinct stages. Furthermore, the properties of the rock mass were calculated and validated against empirical formulas derived from established engineering rock mass classification systems. The findings revealed that the DFN model accurately captures the impact of fracture development on the deformation modulus of rock masses. The orientation of fractures was found to significantly influence the mechanical properties of the rock mass, and the patterns of fracture expansion and connectivity emerged as crucial factors affecting rock properties. This methodology allows for a more accurate calculation of the mechanical characteristics of the rock mass, providing reliable parameters for engineering design.

**Keywords** Discrete fracture network (DFN) · Rock mass properties · Compression damage process · Finite-discrete element method (FDEM)

## Introduction

Natural rock masses are typically intersected by a variety of discontinuities, including fractures, faults, and bedding planes. These discontinuities, with their distinct types, sizes, apertures, and fillings, exert a significant influence on the mechanical behavior of rock masses (Goodman 1991; Priest 1993). They are key determinants of the rock mass's strength, deformation characteristics, seepage properties, and failure modes (Barton 1978). Traditional survey methods for rock mass fractures include the scanline method (La Pointe and Hudson 1985; Wang 2005), the window sampling method (Pahl 1981; Mauldon et al. 2001; Rohrbaugh et al. 2002; Zeeb et al. 2013; Casini et al. 2016), and virtual outcrop technology (Sturzenegger and Stead 2009). Field studies often lead to the derivation of fracture modeling parameters through statistical analysis and description of the geometric distribution and spatial relationships of rock mass fractures (Cardona et al. 2021; Mauldon et al. 2001; Dershowitz and Herda 1992; Zhang and Einstein 2000), which in turn facilitate the creation of a fracture system model (Baecher 1983; Dershowitz and Einstein 1988; Lavoine et al. 2020). The discrete fracture network (DFN) model has gained widespread acceptance for characterizing fracture systems in rock masses (Baecher 1983; Andersson et al. 1984; Elmo and Stead 2009). This model conceptualizes the rock mass as a composite medium comprising discrete fractures and rock blocks, thereby enabling the consideration of fracture characteristics such as spatial distribution, connectivity, and permeability (Davy et al. 2013; Ivars et al. 2021).

Over the past few decades, several geomechanical classification systems have been developed, including the rock mass

✉ Hui Deng
  dh@cdut.edu.cn

  Ming Li
  limingboy@outlook.com

  Guoxing Tu
  pyk@cdut.edu.cn

1   State Key Laboratory of Geohazard Prevention
    and Geoenvironment Protection, Chengdu University
    of Technology, Chengdu 610059, China

rating (Bieniawski 1973), rock quality designation (Deere 1963; Sen and Kazi 1984; Priest and Hudson 1976), geological strength index (Hoek 1983), tunneling quality index (Barton et al. 1974), and the Chinese rock mass basic quality (Standards for Engineering Classification of Rock Mass GB/T50218-2014). These systems have served as the basis for empirical equations proposed by scholars to estimate the deformation modulus of rock masses (Read et al. 1999; Barton 2002). However, the complex influence of fractures within rock masses on deformation parameters such as the elastic modulus and Poisson's ratio has not been adequately addressed in previous research (Wu et al. 2022). The DFN method offers a means to calculate the elastic modulus and Poisson's ratio of rock masses while accounting for the anisotropy of the rock mass and the spatial variability of fractures.

Although rock mass classification systems and empirical relationships are commonly employed in rock mechanics and geological engineering, they often fall short in comprehensively and accurately representing the anisotropic nature of rock masses (Gottron and Henk 2021). The DFN modeling approach provides significant advantages in the study of rock mechanical parameters, particularly in the context of anisotropy. By incorporating the various cracks and faults present in real rocks, the DFN modeling method enables a more realistic simulation of actual rock masses, which is essential for accurately capturing their anisotropic behavior. Moreover, it facilitates the derivation of precise deformation modulus values for rocks.

In this study, we quantify the distribution characteristics, geometry, and spatial relationships of fractures in a rock mass through detailed adit logging surveys. Subsequently, a discrete fracture network model is established to investigate the mechanical properties and parameters of the rock mass across different orientations using compression tests. To verify the accuracy of our findings, we compare the calculated parameters with those obtained using traditional rock mass classification methods. Our analysis uniquely incorporates the spatial variability of primary fracture networks, providing a precise elucidation of the destruction mechanism and mechanical behavior during rock mass failure.

## Fundamentals

### DFN modeling

Statistical methods for characterizing rock mass fractures are essential quantitative tools used to describe and analyze the distribution characteristics, geometry, and spatial relationships of fractures within rock masses. These methods are crucial for evaluating the mechanical and hydraulic properties of rock masses, simulating the failure process of rock masses, and optimizing design and construction in geotechnical engineering (Cardona et al. 2021).

A fundamental aspect of establishing a rock mass fracture model is the accurate description of the spatial locations of fractures. Typically, fractures are assumed to be randomly and uniformly distributed throughout the rock mass, with the centroid of each fracture used to characterize its spatial location. The most commonly employed stochastic model for the spatial location of fractures is the Poisson distribution. The orientation of a fracture determines its direction of extension within the rock mass, which is primarily governed by the dip direction, dip angle, and rotation angle. Fractures are usually categorized into different groups based on collected fracture directions, with each subset exhibiting clustered distributions. Most fractures within a subset share the same direction, exhibiting a clear clustering tendency, while the remainder are scattered around this direction. This pattern of distribution is consistent with the Fisher distribution.

The size of a fracture characterizes its extent within the rock mass and is a critical parameter affecting the integrity and mechanical properties of the rock mass. Typically, fracture size adheres to a power-law distribution, where the exponent of the power law is key to describing the shape of the fracture size distribution. Different rock types and geological conditions can lead to varying power-law exponents.

The complexity of the fracture network is primarily governed by the fracture intensity. Dershowitz and Herda (1992) introduced measures such as $P_{10}$, $P_{20}$, $P_{21}$, $P_{30}$, and $P_{32}$ to quantify fracture density in one, two, and three dimensions (Fig. 1). In this study, the $P_{ij}$ system will be utilized to quantify fracture intensity.

## Simulation of rock compression using PCDC2D

The parallel continuum discontinuum code (PCDC2D) is a sophisticated numerical simulation tool that integrates macromechanics and micromechanics through a hybrid finite-discrete element method (FDEM). This approach combines the strengths of the finite element method (FEM) and the discrete element method (DEM), providing an effective means to address the complexities of solid structures with intricate interfaces and fracturing behaviors. In the present study, PCDC2D is employed to conduct rock compression tests, calculate rock mass parameters, and explicitly simulate the deformation and damage processes of a jointed rock mass. This includes the simulation of tensile and shear damage modes of fractures, as well as the propagation, penetration, and the initiation, growth, and penetration of new fractures within intact rock masses.

### Intrinsic cohesive zone model

The cohesive zone model (CZM) is a fracture mechanics model that conceptualizes fracture formation as a progressive process. By utilizing the CZM, it is possible to predict

| | Dimension of Fracture Measure | | | |
| --- | --- | --- | --- | --- |
| Dimension of Sampling Region | 0 (number) | 1 (length) | 2 (area) | 3 (volume) |
| 1D line | $P_{10}$ Fracture intensity | $P_{11}$ Fracture porosity | | |
| 2D area | $P_{20}$ Fracture density | $P_{21}$ Fracture intensity | $P_{22}$ Fracture porosity | |
| 3D volume | $P_{30}$ Fracture density | | $P_{32}$ Fracture intensity | $P_{33}$ Fracture porosity |

**Fig. 1** The $P_{ij}$ system, adapted from Dershowitz and Herda (1992), is utilized for deriving input parameters in DFN modeling

the initiation and propagation of fractures and to obtain a detailed depiction of the fracture growth process in pre-existing fractures within a rock mass (Alfano et al. 2009). The CZM offers significant advantages in simulating the direction of fracture propagation in rocks, making it a suitable choice for this study to simulate the generation and extension of fractures in a rock mass. In the CZM, the normal stress $\sigma_{coh}$ and shear stress $\tau_{coh}$ at the fracture surface are determined by Eqs. (1) and (2), respectively.

$$\sigma^{coh} = \begin{cases} \frac{2o}{o_{overlap}} T_s & \text{if } o < 0 \\ \left[\frac{2o}{o_p} - \left(\frac{o}{o_p}\right)^2\right] f(D)T_s & \text{if } 0 \leq o \leq o_p \\ f(D)T_s & \text{if } o_p < o \end{cases}$$

(1)

$$\tau^{coh} = \begin{cases} \left[\frac{2|s|}{s_p} - \left(\frac{|s|}{s_p}\right)^2\right](-\sigma^{coh}\tan(\varphi) + f(D)c) & \text{if } 0 \leq |s| \leq s_p \\ -\sigma^{coh}\tan(\varphi) + f(D)c & \text{if } s_p < |s| \end{cases}$$

(2)

In the cohesive zone model (CZM), the parameters $\varphi$ and c denote the angle of internal friction and the cohesion of the rock material, respectively. The symbol $T_s$ represents the tensile strength of the rock. The normal opening, $o_p$, and shear displacement, $s_p$, define the critical thresholds at which fractures transition from elastic deformation to strain softening, with op representing the critical normal opening and $s_p$ representing the critical shear displacement. The variables o and |s| denote the actual fracture opening and shear displacement, respectively. The function f(D) characterizes the softening behavior of fractures as a function of their opening and shear displacement, with D representing the rupture factor. This factor, along with the function f(D), is utilized to account for both Type I (tensile) and Type II

(shear) rupture modes, as well as mixed-mode I-II rupture modes, thus providing a comprehensive model for fracture behavior in rocks (Mahabadi et al. 2012).

$$D = \begin{cases} \text{Minimum}\left(1, \sqrt{\left(\frac{o-o_p}{o_t}\right)^2 + \left(\frac{|s|-s_p}{s_t}\right)^2}\right) & \text{if } o \geq o_p \text{ or } |s| > s_p \\ 0 & \text{if } o < o_p \text{ And } |s| \leq s_p \end{cases}$$

(3)

$$f(D) = \left[1 - \frac{A+B-1}{A+B}\exp\left(D\frac{A+CB}{(A+B)(1-A-B)}\right)\right][A(1-D) + B(1-D)^c] (0 \leq D < 1.$$

(4)

where A, B, and C are coefficients that determine the shape of the softening curve. These coefficients are generally established through laboratory tests. However, numerical calculations have revealed that the precise shape of the softening curve has a minimal impact on the overall calculation outcomes. Consequently, in this study, A, B, and C are treated as constants, with assigned values of 0.63, 1.8, and 6.0, respectively. The parameters $o_t$ and $s_t$ represent the ultimate critical values for tensile and shear displacements, beyond which the fracture's behavior is characterized by macroscopic fracturing.

## PCDC exact method of DFN model generation

The process of generating a DFN model within PCDC involves several steps. Initially, the geometrically defined fractures from the DFN model are extracted and imported into the software. Subsequently, using PCDC commands and considering these geometric fractures along with the model boundaries, the model mesh is constructed. This is followed by the identification and naming of the fracture groups within the model. Finally, appropriate constitutive relationships and corresponding mechanical parameters are assigned to the fractures in the model.

## Rock mass classification schemes

The rock quality designation (RQD) scheme, introduced by Deere in 1963, quantifies the proportion of core samples longer than 10 cm in relation to the total core length. Alternative methods for assessing RQD include the use of empirical formulas and statistical distributions, which analyze the intervals between fractures (Sen and Kazi 1984; Zhang 2016; Priest and Hudson 1976). For example:

$$RQD = 100e^{-0.1\lambda}(0.1\lambda + 1). \tag{5}$$

where $\lambda$ represents the average number of discontinuities per meter.

The rock mass rating (RMR) is a geological rock mechanics classification system, which was established by Bieniawski in 1973. The formula for calculating the RMR is as follows:

$$RMR = \left(R_1 + R_2 + R_3 + R_4 + R_5\right) + B. \tag{6}$$

The RMR method's initial value is determined by incorporating five key parameters: rock strength ($R_1$), rock quality designation (RQD) ($R_2$), fracture spacing ($R_3$), fracture roughness ($R_4$), and groundwater conditions ($R_5$). Following the establishment of the initial value, it is subsequently adjusted based on the score ($B$) that reflects the relationship between the fracture surface yield and the adit.

Building upon this foundation, Barton et al. (1974, 2002) drew upon a comprehensive suite of case studies pertaining to underground cavern excavation to introduce the Q-System, a tunneling quality index. This index is expressed as:

$$Q = \left[\frac{RQD}{J_n}\right] \times \left[\frac{J_r}{J_a}\right] \times \left[\frac{J_w}{SRF}\right]. \tag{7}$$

Where $J_n$ represents the number of fracture groups, $J_r$ represents the fracture roughness number, $J_a$ represents the fracture alteration number, $J_w$ represents the fracture water reduction factor, and SRF represents the stress reduction factor.

## Workflow

Figure 2 illustrates the research workflow for determining the deformation modulus of a rock mass utilizing the DFN model and for the classification of an engineered rock mass. This workflow encompasses both field survey work and laboratory testing. The fieldwork component involves detailed cataloging of fractures within the adit, including the documentation of fracture orientation, intensity, size, filler material, and shape. These data are crucial for generating the DFN model and for acquiring the evaluation indices necessary for the classification of the engineering rock mass quality. Laboratory tests are subsequently conducted on rock samples collected from the field. These tests include uniaxial and triaxial compression tests to determine the rock's mechanical properties and direct shear tests on fracture surfaces to assess their shear strength characteristics.

Once the DFN model is constructed, numerical simulation software is employed to calculate the rock mass properties. This is achieved by integrating the mechanical parameters of the rock and fracture surfaces obtained from the laboratory tests. Fracture propagation and penetration modes
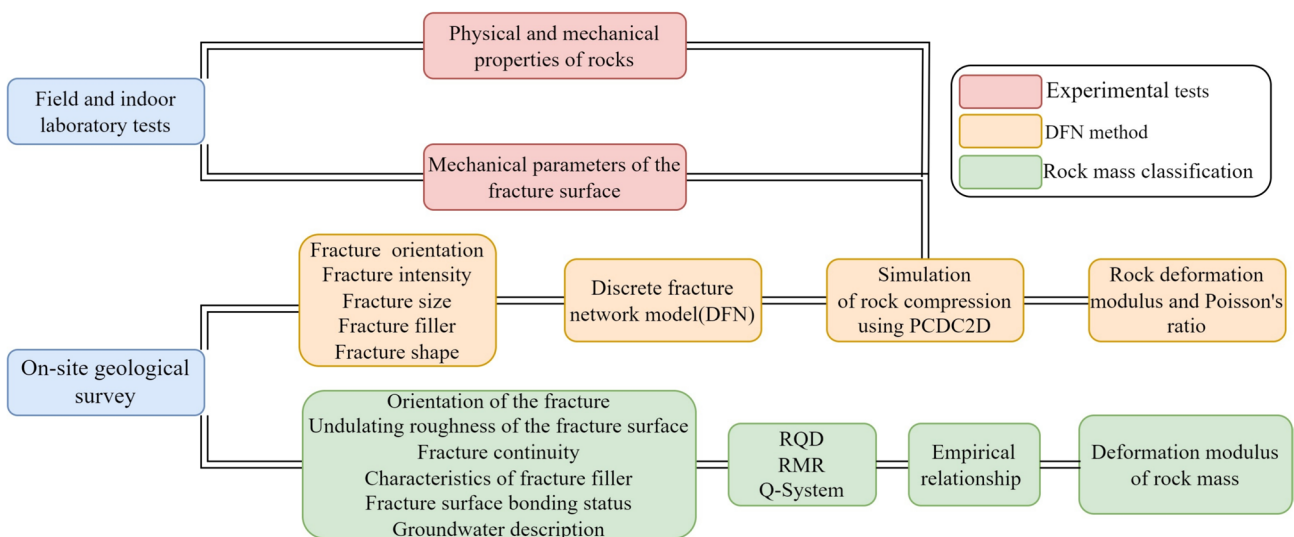


**Fig. 2** Workflow for determining the mechanical properties of rock bodies using DFN modeling methods and rock mass classification

are then analyzed using fracture mechanics principles. Finally, the rock mass deformation modulus is estimated through the application of engineering rock classification systems and empirical relationships. This estimation serves to validate the accuracy of the DFN modeling approach.

## Geologic setting and data acquisition

### Case study research

The primary objective of this study was to determine the rock mass parameters for an underground powerhouse. To this end, the underground powerhouse of the GS Hydropower Station was selected as the focal point of the research. The GS power station's dam site is situated in the upper reaches of the Lancang River within Deqin County, Yunnan Province. The river's course exhibits a near-flat S-shaped configuration, characterized by swift water flow. The underground powerhouse is positioned within the rock mass on the river's right bank, with an axial direction of SW200° (S20°W). It is deeply buried, with the main structure situated in the $P_1j^3$ member of the Lower Permian Jidonglong Formation (Fig. 3). The lithology of the stratum hosting the powerhouse predominantly consists of basaltic rock. The main adit, PD4, is located at an elevation of 2094 m and extends 700 m in length, with three branch adits traversing the entire research area.

The rock mass exposed within the underground powerhouse is characterized by blocky basalt (Fig. 4), with a well-developed fracture network. Apart from the F1 fault located in the upper reaches of the Lancang River, no major faults are evident in the dam site area. The small faults present are relatively narrow, and the connectivity and aperture of the fracture groups exhibit similarities, facilitating the reasonable establishment of a DFN model. Additionally, the rock mass in the study area is complex fractured, and utilizing the DFN method to simulate the rock mass provides detailed information about the fracture structure and allows for full consideration of the role of hidden micro-fractures within the rock mass.

### Field data collection

For the purposes of this study, extensive data were gathered through continuous measurements in adit PD4, employing the universal survey network method. This process yielded a total of 805 fractures of various types, which were meticulously documented. Based on this data, a typical adit display map was constructed (Fig. 5), with Figs. 5(a) and 5(b) illustrating the fracture mappings at depths ranging from 300–400 m and 500–600 m, respectively.

Rock samples were meticulously collected from the field and transported to the laboratory for a comprehensive suite of rock mechanics tests, including triaxial compression, direct tensile, and shear tests (Fig. 6(b, c)). These tests yielded detailed mechanical parameters for the primary lithologies within the study area, as presented in Table 1.

Drawing upon the field exploration of the adit rock mass, the outcomes of in situ fracture shear tests (Fig. 6(a)), laboratory experimentation (Fig. 6(c)), and the insights provided by the research conducted by Zheng et al. (2024a, b), the mechanical parameter values for the fractures were meticulously determined (Table 2).

## Modeling approach

### DFN modeling

The on-site adit logging data were meticulously analyzed to ascertain the predominant orientation, size, intensity, and other essential characteristics of the fractures within the rock mass enveloping the underground powerhouse in the study area. Fracture nodal poles exhibited a trend of clustering within specific subzones, displaying a high degree of density. To characterize the spatial distribution of natural fracture orientations, the Fisher function was employed, leading to the generation of an iso-density map that adheres to probabilistic statistical principles (Fig. 7). The fracture poles were grouped into several zones, and for each group, the inclination, trend, and kappa values of the Fisher function were determined (Table 3).

Statistical analysis of the PD4 adit logging and fracture length data (Fig. 5) yielded a distribution curve of fracture trace lengths (Fig. 8). In this figure, the horizontal axis represents fracture size, while the vertical axis denotes cumulative density. It is observed that smaller fractures exhibit less dispersion in mean values and a denser data distribution, whereas larger fractures show greater dispersion in mean values and a wider data distribution. Overall, the fracture size distribution follows a power-law pattern.

Building upon the extensive field survey of the rock mass within the adit, a substantial dataset on fractures was compiled, revealing the distinctive characteristics of the rock mass's fracture network (Fig. 5). To establish an accurate DFN model reflective of the study area, it was necessary to estimate the fracture intensity from the adit sampling fracture trace data. Given that the surveyed adit approximates a flat, cylindrical shape, the volumetric fracture intensity of the rock mass, $P_{32}$ (fracture area per unit of rock volume), is related to the areal fracture intensity on the cylindrical surface, $P_{21,D}$ (fracture trace length per unit of sampled surface area). This relationship is expressed through the general conversion factor definition ($C_{23,D}$):
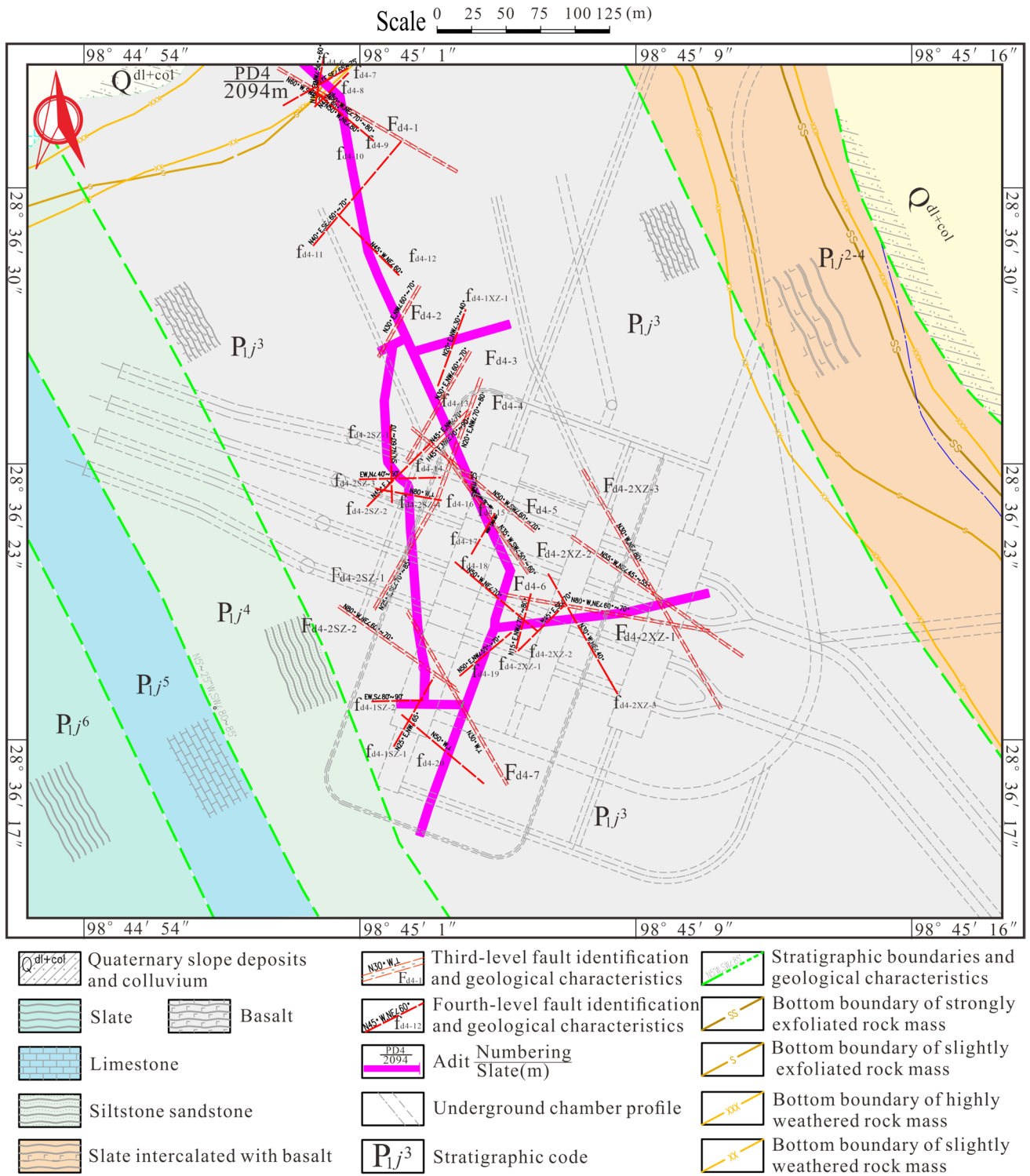
**Fig. 3** Geological and adit placement map at an elevation of 2110 m in the study area

$$p_{21,D} = \frac{K * \sum l_i}{A},$$

(8)

Where $\sum l_i$ is the sum of the fracture traces within the logging area, $A$ represents the area of the fracture logging area, $K$ is the statistical fracture trace amplification factor (acknowledging the limitations inherent in field logging), and $P_{21,D}$

**Fig. 4** PD4 rock mass in adit: (**a**) 5 m inside the adit, and (**b**) 300 m inside the adit
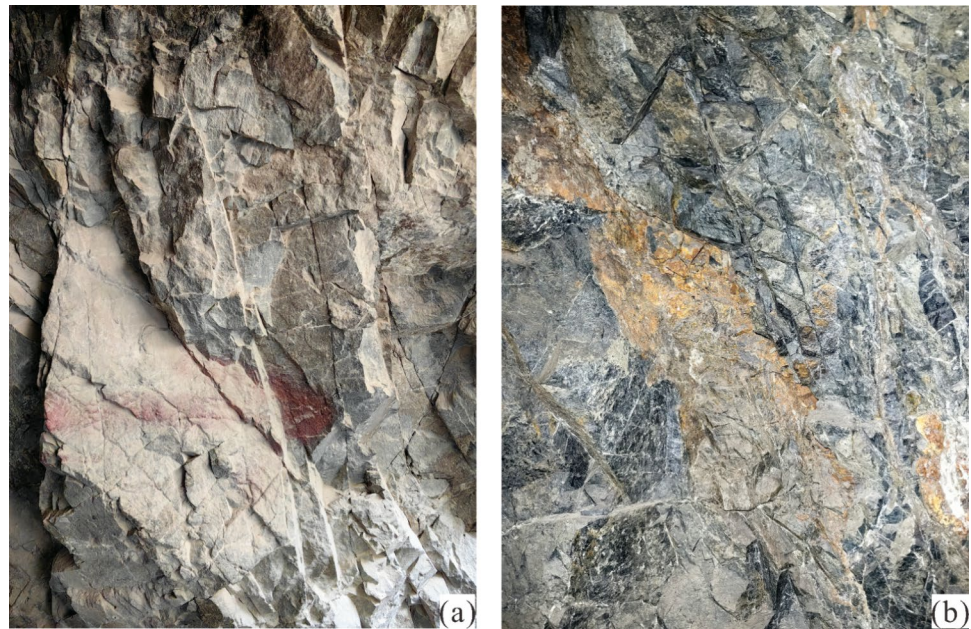


denotes the measured fracture intensity in the logging area (the length of fracture traces per unit of sampled surface area).

$$P_{32} = C_{23,D} P_{21,D}, \tag{9}$$

The subscript 23 indicates the conversion from a 2-D to a 3-D measurement dimension, while the subscript D refers to the columnar surface sampling domain. Drawing upon the findings of Wang (2005), the conversion factor ($C_{23,D}$) is suggested in conjunction with the adit logging survey conducted in the study area:

$$C_{23,D} = \frac{3\pi}{2} \left[ \int_{\theta=0}^{\theta=\frac{3\pi}{2}} \int_{\beta=0}^{\beta=\frac{\pi}{2}} \int_{\alpha=0}^{\alpha=\frac{3\pi}{2}} \frac{\sin\beta}{2\pi} \sqrt{\cos^2\beta + \sin^2\beta \sin^2(\theta-\alpha)} \, d\alpha \, d\beta \, d\theta \right]^{-1}. \tag{10}$$

The total length of the fracture traces within the adit's rock mass is denoted as $\sum l_i = 2627.72$ m, and the area of the logged rock mass is A = 7197.39 m². Considering the field survey and the degree of fragmentation of the rock mass, an amplification coefficient for the fracture traces of K = 2.0 is adopted. Substituting this value into Eq. (8) yields $P_{21,D}$, which can then be used in Eq. (9) to calculate $P_{32}$. The calculated results are presented in Table 3.

## PCDC2D model input parameters

The numerical model employs the Mohr–Coulomb constitutive model, with the specific parameters adjusted in accordance with the outcomes of the laboratory rock mechanics tests (Table 1). The final set of parameters is detailed in Table 4.

To simulate the rupture process of materials, the parallel continuum discontinuum code (PCDC) establishes fracture cells between adjacent cells of the finite element mesh. These fracture cells are governed by the cohesive zone model (CZM), which is known for its capability to accurately predict the deformation and damage behavior of rock masses (refer to Sect. "Rock mass classification schemes" for details). Numerical experiments have indicated that the penalty stiffness parameters ($P_{open}$, $P_{tan}$, $P_{overlap}$) should be set to values ranging from 10 to 100 times the Young's modulus of elasticity of the finite element cell, as suggested by Wang et al. (2018), Yao et al. (2022), Zhou et al. (2021, 2015). The precise parameter values are provided in Table 5.

## Deformation modulus estimation methods based on rock mass classification

Empirical equations have been extensively developed through prior rock engineering research. This study aims to estimate the deformation modulus of a rock mass using various rock mass classification systems, including the rock mass rating (RMR), Q-System, and rock quality designation (RQD). The objective is to compare these estimates with those obtained using the discrete fracture network (DFN) method to verify the accuracy of the DFN approach. Table 6 outlines the empirical relationships between the different rock mass classification systems and the deformation modulus of the rock mass. The estimation of the deformation modulus involves compiling and organizing parameters from various systems while integrating field data and test outcomes.
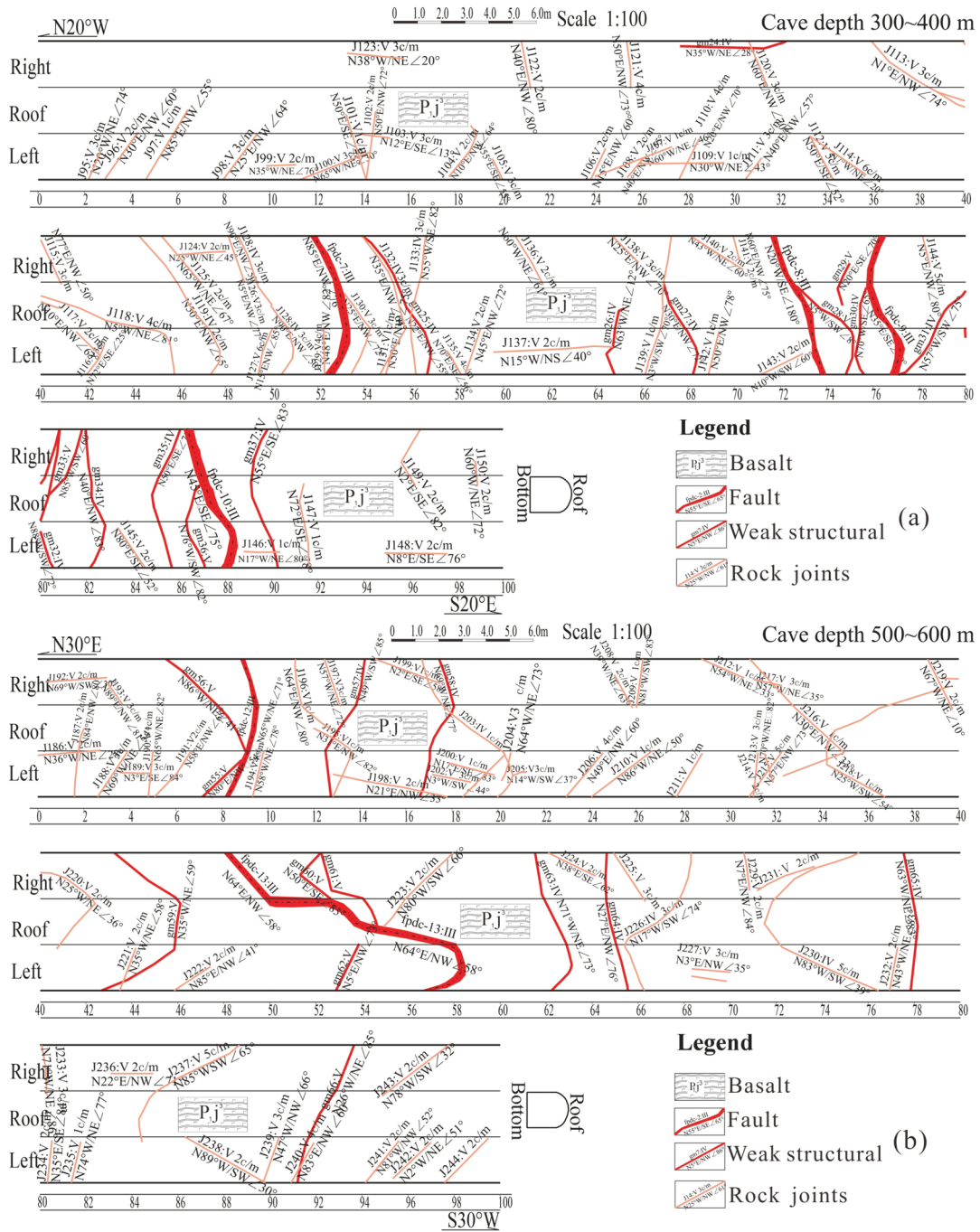
**Fig. 5** PD4 adit rock mass logging maps. (**a**) Rock wall display for adit depths of 300–400 m, and (**b**) Rock wall display for adit depths of 500–600 m

## Results

### Validation of DFN model

A comprehensive survey was conducted within the underground powerhouse area of the GS Power Station, utilizing an adit to gather raw data on fracture parameters. From this data, key modeling parameters such as the dip direction, dip angle, and intensity ($P_{32}$) for each fracture group in the study area were determined (Table 3). A model was developed to characterize the power law parameters of fracture length. Subsequently, DFN.lab (Lavoine et al. 2020) was employed to perform discrete fracture network fitting for the fractured rock masses in the study area.

**Fig. 6** Experimental tests, (**a**) field fracture shear test, (**b**) laboratory rock triaxial test, (**c**) laboratory rock shear test
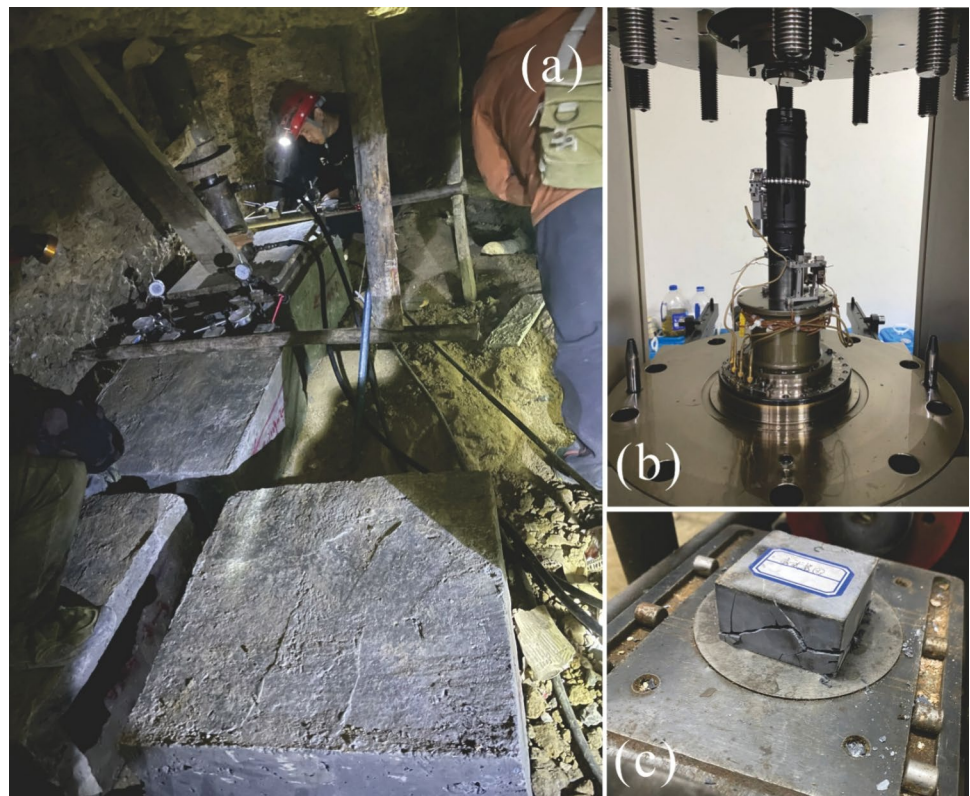


**Table 1** Physical and mechanical properties of rocks

|  | Density (kg/m$^3$) | Compressive strength (MPa) | Tensile strength (MPa) | Elastic modulus ($E_m$) (GPa) | Deformation modulus ($E_0$) (GPa) | Poisson's ratio (v) |
|---|---|---|---|---|---|---|
| Basalt | 2700 | 130 | 7.5 | 50 | 36 | 0.24 |

Under consistent rock structure conditions, the size of the rock mass significantly influences its mechanical parameters. Current research suggests that the Representative Elementary Volume (REV) could extend up to 5–10 times the fracture spacing (González-Fernández et al. 2024; Schultz 1996). The DFN model employed in this study has dimensions of 40 m × 40 m × 40 m (Fig. 9), with a fracture spacing of less than 1.2 m, thereby ensuring that the mechanical parameters of the rock mass remain consistent across different volumes. To assess the model's validity, a comparison was made between the cumulative density distribution curves of the generated model and the fracture lengths from the input power law parameters. The comparison revealed a significant discrepancy between the extremes and a close alignment in the middle (Fig. 10). Overall, the DFN model provided a reliable simulation of the rock mass in the study area.

## Determination of rock mass parameters and extension and penetration of fractures based on numerical modeling

Advancements in rock mass behavior research under stress and fracture conditions have been made through various studies (Zhang and Zhou 2020; Zhang et al. 2024, 2023; Zhou et al. 2019). In this study, a consistent model size was used to eliminate the influence of size effects, enhancing the comparability of experimental results. By altering the loading direction, the stress–strain behavior of the

**Table 2** Mechanical parameters of the fracture surface

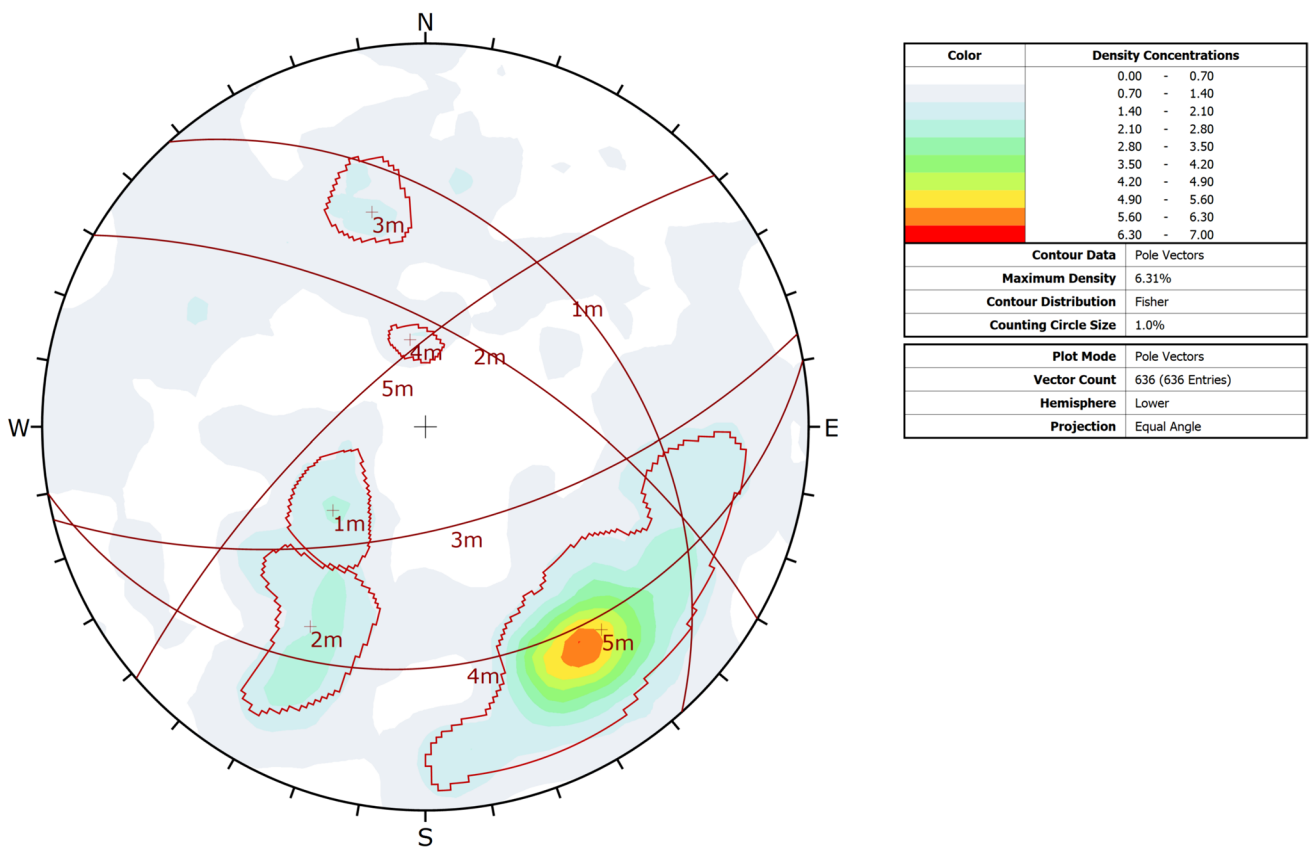| Type of fracture surface | Peak intensity | | Residual intensity | |
|---|---|---|---|---|
|  | Friction ($\varphi'$) (°) | Cohesive(C') (MPa) | Friction ($\varphi$) (°) | Cohesive (C) (MPa) |
| Rigid fracture surfaces (joints) | 30 | 0.50 | 30 | 0.30 |

**Fig. 7** Fisher distribution iso-density plot of fracture poles

**Table 3** Geometric properties of the fractures in PD4

| Serial number | Dip direction (°) | Dip (°) | Fisher K | $P_{21,D}$ | $P_{32}$ |
|---|---|---|---|---|---|
| 1 | 228.31 | 54.50 | 65.8429 | 0.114 | 0.147 |
| 2 | 210.44 | 28.05 | 48.3848 | 0.159 | 0.205 |
| 3 | 346.14 | 29.89 | 136.867 | 0.045 | 0.059 |
| 4 | 349.75 | 63.96 | 463.147 | 0.023 | 0.029 |
| 5 | 138.58 | 19.59 | 15.1909 | 0.513 | 0.662 |

rock mass was observed in different orientations, providing insights into the anisotropic performance and damage process of the rock mass.

To accurately simulate the deformation and damage process of the rock mass, as well as its anisotropy, and to observe fracture growth, extension, and penetration phenomena, the middle section of the generated DFN model (Fig. 9) was used as the geometric boundary and fracture geometry. Based on the rock parameters established in Tables 4 and 5, the internal cohesive zone model, and the PCDC procedure, a DFN test model with dimensions of 40 m × 40 m was constructed (Fig. 11). Displacement walls were applied to the upper and lower parts of the model to conduct a series of uniaxial compression tests. For the boundary conditions under uniaxial compression tests, the axial displacement load was consistently applied parallel to the coordinate axes (up and north axes) on the model surface. When loading vertically (Fig. 11(a)), the displacement load was parallel to
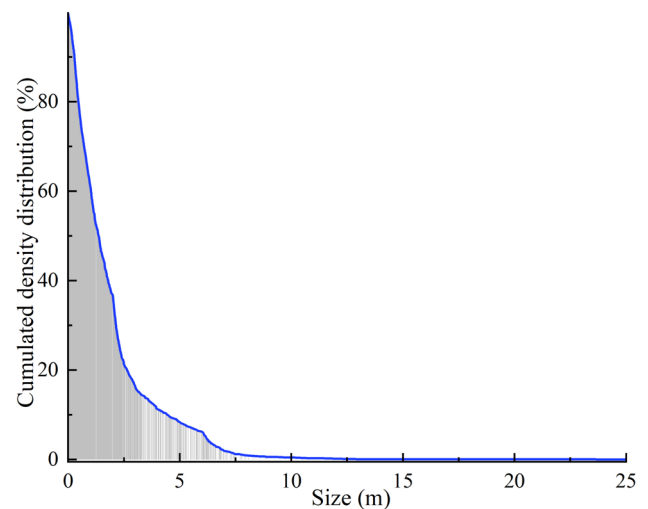


**Fig. 8** Density distribution of fracture lengths in adit PD4

**Table 4** Mohr–Coulomb elastic–plastic constitutive model input parameters

| Parameters | Density | Young's modulus | Poisson ratio | Penalty | Damp factor |
|---|---|---|---|---|---|
| Symbol | $\rho$ (kg/m$^3$) | $E_m$ (Pa) | $v$ | $P$ | $D_f$ |
| Value | 2700 | 5e10 | 0.24 | 5e10 | 1.0 |

the up direction, with the horizontal direction (north) unrestricted; conversely, when loading horizontally (Fig. 11(b)), the displacement load was parallel to the north direction, with the horizontal direction (up) unrestricted.

The stress–strain curves for both vertical and horizontal compression tests were obtained (Fig. 12). As illustrated in Fig. 12, the anisotropy of the rock mass is evident, with the stress value being significantly lower for the vertical model (with the up axis upward) compared to the horizontal model (with the north axis upward) after the vertical model reaches its peak strength. However, the overall trend of the stress–strain curves is consistent between the two models, which is corroborated by the fracture development during the deformation process (Figs. 13(a–c)). Figures 13(d–f) depict the fracture extension process for the vertical model. Based on the stress–strain curves and the fracture development, the compression damage to the rock mass was categorized into the following four stages:

1) Fracture Compaction Stage: The internal fractures within the rock mass generate local friction, corresponding to the portion of the stress–strain curve prior to the first turning point. The strain change is minimal, and the stress increases rapidly. The rock mass as a whole is in the elastic deformation stage, with no apparent damage to the rock mass and no new fractures being produced.

2) Transition from Elastic to Plastic Deformation and Microplastic Fracture Stabilization: During this stage, the axial stress initially decreases with increasing com-
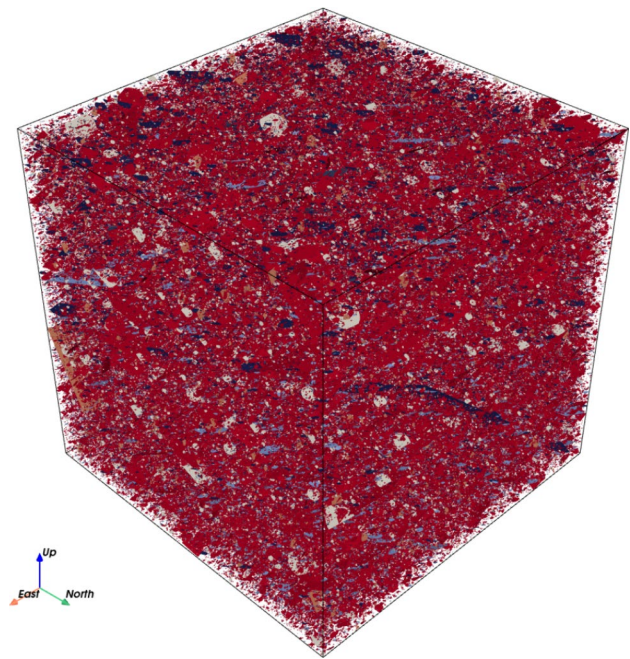


**Fig. 9** Effective DFN computational model generated

pression before exhibiting a tendency to increase as the rock mass deforms further, eventually reaching a peak value. Figures 13(a) and (d) illustrate the deformation of the rock mass for the horizontal and vertical models, respectively, at this stage of fracture development. At the ends of the pre-existing fractures, microfractures nucleate and develop into tension and shear fractures. While the number of nascent fractures is relatively low, the primary direction of fracture propagation is still influenced by the growing fractures, with sprouts emerging from the ends of one set of pre-existing fractures and extending towards another set at the intersection.

3) Unstable Fracture Propagation Stage: Following the peak in axial stress, under vertical compression, tensile

**Table 5** Input parameters for the internal cohesive zone model of fracture units

| Parameters | Friction | Cohesion | Tensile strength | Type I fracture energy | Type II fracture energy | Penalty overlay | Penalty normal | Penalty shear |
|---|---|---|---|---|---|---|---|---|
| Symbol | $\varphi$ (°) | $C$ (Pa) | $T_s$ (Pa) | $G_{f1}$ (N/m) | $G_{f2}$ (N/m) | $P_{overlap}$ (Pa) | $P_{open}$ (Pa) | $P_{tan}$ (Pa) |
| Value | 30 | 10e6 | 1.5e6 | 500 | 5000 | 2.5e14 | 2.5e13 | 2.5e13 |

**Table 6** Various empirical relationships for determining the deformation modulus of a rock mass

| Publication | Classification System | Equation |
|---|---|---|
| Zhang and Einstein 2004 | RQD | $\dfrac{E_m}{E_i} = 10^{0.0186RQD - 1.91}$ |
| Galera et al. 2007 | RMR | $E_m = E_i e^{\frac{(RMR-100)}{36}}$ |
| Ajalloeian and Mohammadi 2013 | Q-System | $E_m = -0.016Q^2 + 1.581Q + 0.961$ |

**Fig. 10** DFN model fracture length distribution
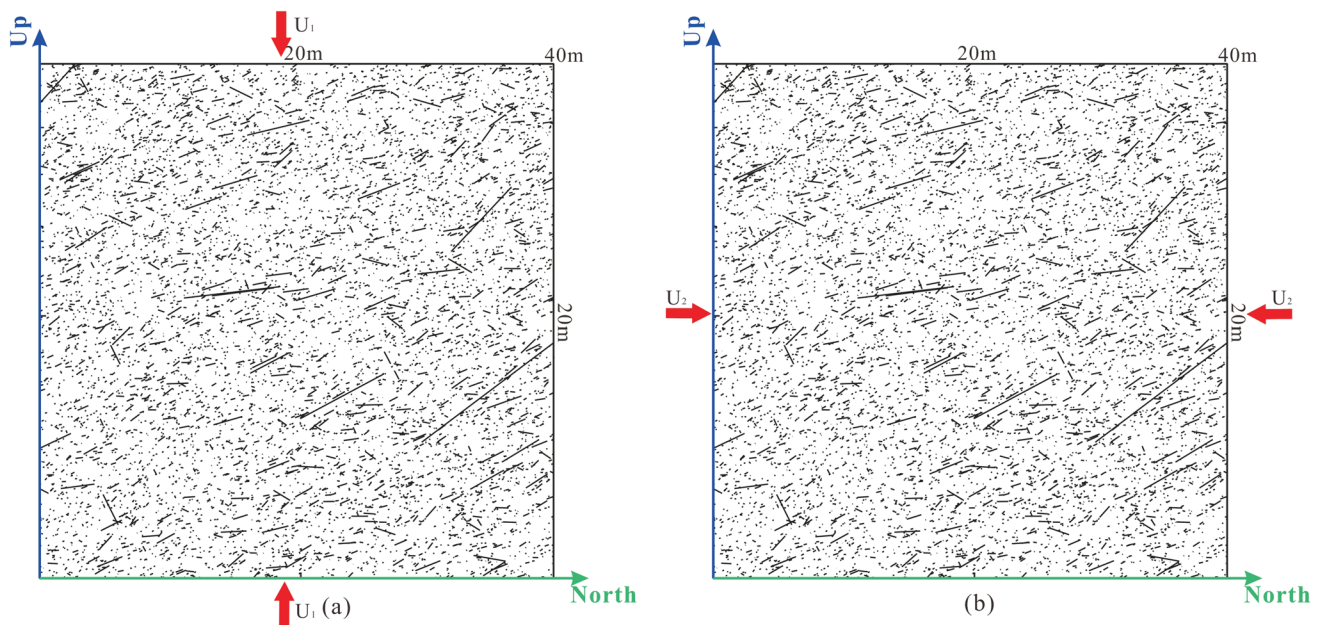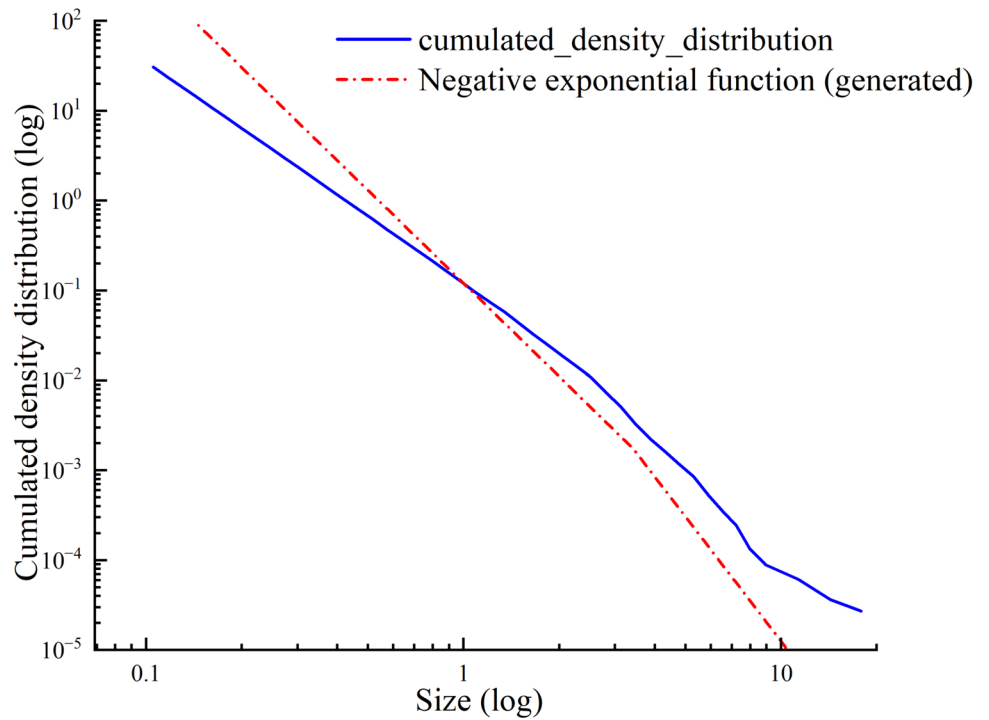


**Fig. 11** Schematic diagram of the uniaxial simulation using PCDC2D: (**a**) vertical compression, and (**b**) horizontal compression

and shear fractures within the rock mass undergo significant expansion (Figs. 13(b) and (e)). In the vicinity of the fractures formed in the previous stage, the rock mass continues to rupture, with nuclei expanding to the periphery. The form of destruction differs from that of intact rock, typically manifesting as the emergence of

secondary fractures and rapid expansion. The stress–strain curves exhibit step-like undulations.

4) Post-Rupture Stage: The stress decreases sharply with increasing strain, and the fractures propagate to form the primary crack, leading to the overall instability of the rock specimen. For the same specimen, the loading

**Fig. 12** Stress–strain curves of rock mass under uniaxial compression
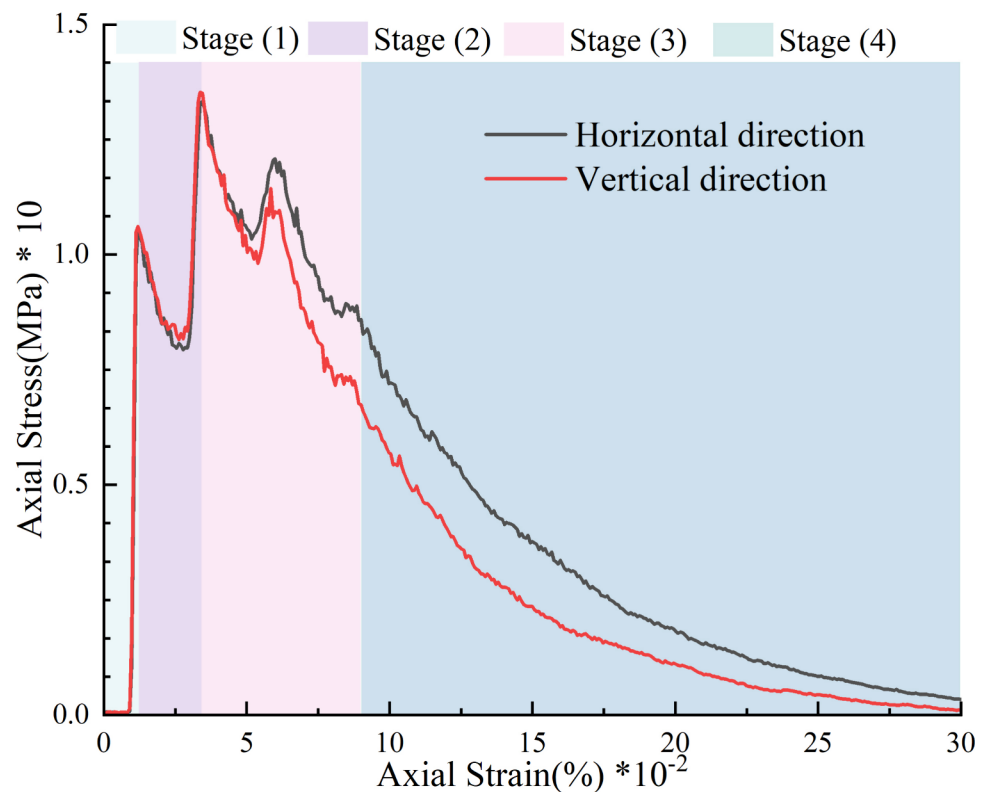


direction results in distinct forms of damage (Figs. 13(c, f)). In the vertical loading model, the primary rupture occurs at 45° (relative to 0° in the vertical direction), and the rock mass is fragmented into small and medium-sized clasts by a 135° fracture. In contrast, in the horizontal loading model, the primary rupture is at –45°, with the anisotropy of the rock mass being pronounced (Fig. 14).

According to the analysis presented, during the unstable rupture development stage, the axial stress reaches its peak, after which the fractures rapidly expand, and the rock mass commences plastic deformation. This behavior reflects the overall strength properties of the rock mass.

Consequently, the stress–strain value at this stage is utilized to calculate the deformation modulus of the rock mass. Additionally, the Poisson's ratio of the rock mass is determined by the ratio of lateral strain to longitudinal strain.

$$E_m = \frac{\sigma_3}{\varepsilon_3}. \tag{11}$$

$$v_m = \frac{-\varepsilon_{3,x}}{\varepsilon_{3,z}} \tag{12}$$

Equations (11) and (12) are utilized to estimate the deformation modulus and Poisson's ratio of the rock mass. The deformation modulus for the vertical model (up) is found to vary between 9.98 and 17.82 GPa, while for the horizontal model (north), it ranges from 8.28 to 15.12 GPa. Similarly, the Poisson's ratio for the vertical model (up) lies between 0.27 and 0.31, and for the horizontal model (north), it spans from 0.29 to 0.33.

## Deformation modulus estimation results based on rock mass classification

In classifying the engineering geology of the rocks surrounding the underground powerhouse, the rock type serves as the primary determinant. The stability of the surrounding rock is influenced by several factors, including lithology, fracture orientation, weathering and unloading degree, rock mass structure type, fracture characteristics and patterns, and groundwater activity. By taking these factors into account comprehensively, calculations were conducted to ascertain the RQD, RMR, and Q-System values (Table 7). Specifically, the RQD reflects the fundamental quality of the rock mass, with scores ranging from 75 to 85. The RMR scores are in the range of 53 to 64, and the Q-System scores lie between 25 and 35.
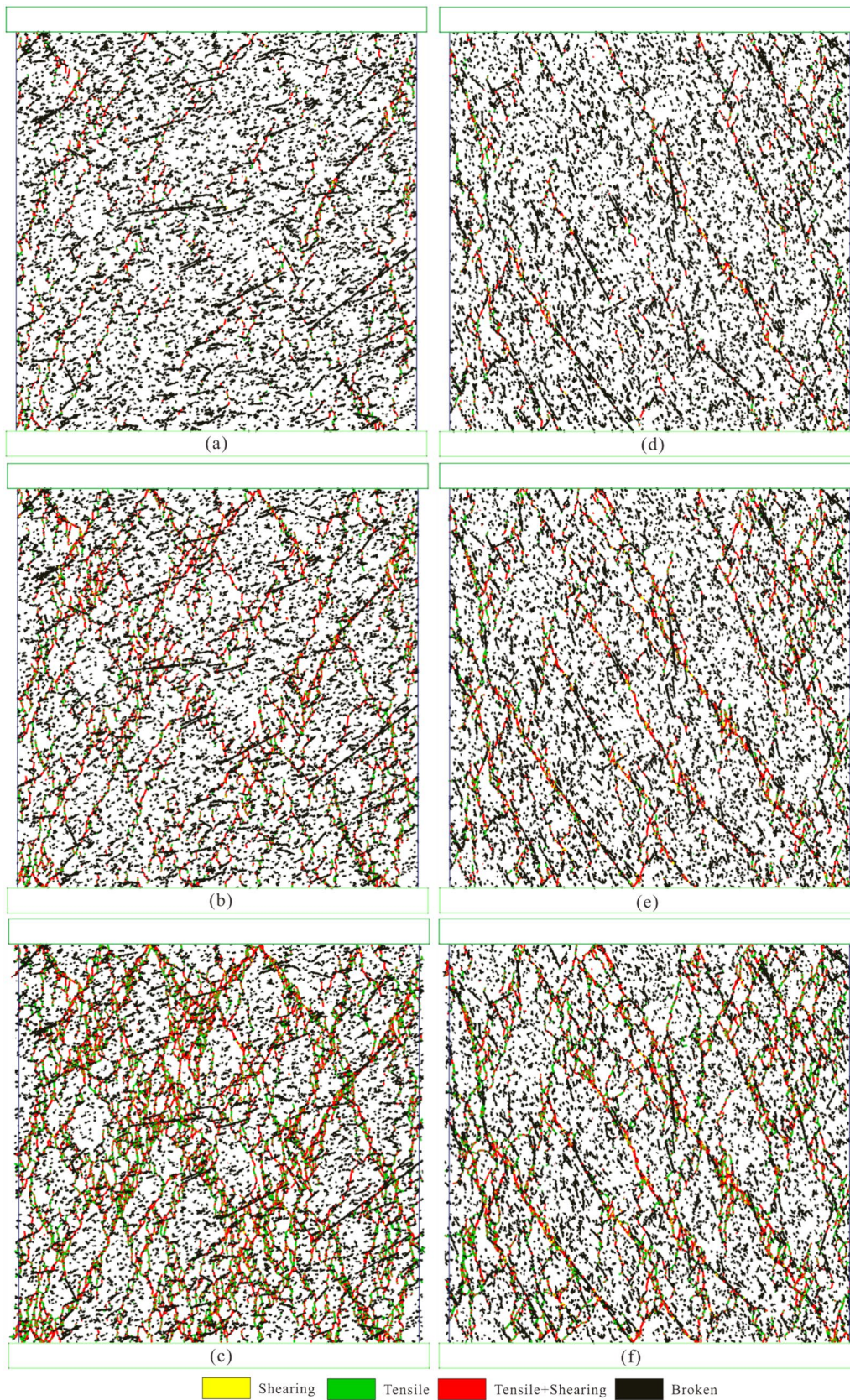
| Shearing | Tensile | Tensile+Shearing | Broken |

**Fig. 13** Forms of fracture generation, extension, and penetration of rock mass under uniaxial compression: (**a–c**) under compression in the vertical direction, and (**d–f**) under compression in the horizontal direction
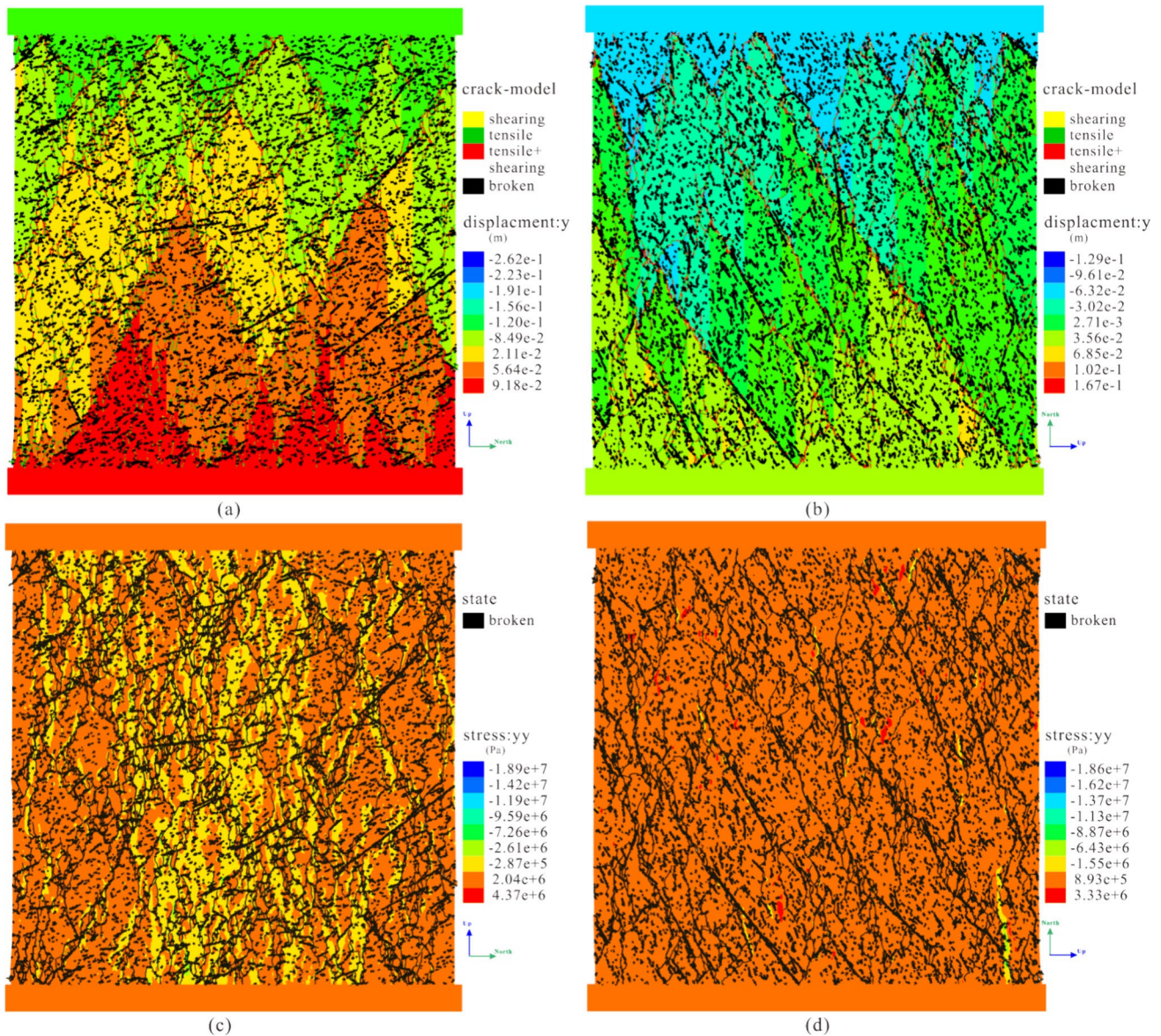
**Fig. 14** The final damage pattern of the rock mass and the development of fractures: (**a**) and (**c**) stress and displacement loaded in the vertical direction, and (**b**) (**d**) stress and displacement loaded in the horizontal direction

Based on the evaluation results presented in Table 7, the corresponding deformation moduli were calculated using the empirical relationships outlined in Table 6. The elastic moduli obtained using the RQD evaluation method and empirical relationship (Zhang and Einstein 2004) range from 15.27 to 23.44 GPa. Those derived using the RMR evaluation method and empirical relationship (Galera et al. 2007) range from 18.18 to 23.04 GPa. Those determined using the Q-system evaluation method and empirical relationship (Ajalloeian and Mohammadi 2013) range from 21.08 to 30.49 GPa (Fig. 15). Overall, the simulation results for the study area exhibit minimal dispersion, with the deformation moduli concentrated between 14 and 24 GPa. The computed deformation moduli of the rock mass based on the DFN model were found to be in good agreement with those obtained using the empirical relationships of other evaluation methods. Notably, the deformation moduli obtained using the Q-system approach were higher than those obtained using the other methods.

**Table 7** Results of the adit survey and rock classification system calculations for the study area

| RQD | RMR | Q-System |
|---|---|---|
| 75–85 | 53–64 | 15–25 |

# Discussion

To ascertain the geometric parameters and spatial distribution of fractures within rock masses, two predominant methods have been widely employed: laser scanning and manual window method logging. Laser scanning offers high-precision data; however, it is costly and technically challenging to operate within confined cave environments, requiring the continuous repositioning of the scanning apparatus. Moreover, the subsequent data processing tasks, such as point cloud stitching and fracture identification, can be prone to high error rates. Conversely, manual logging, while less efficient, allows for the reliable assessment and documentation of fracture size, orientation, and density on exposed cave walls. Therefore, given the considerations of cost-effectiveness, operational complexity, and data accuracy, the manual window method was selected for logging to obtain accurate geometric parameters and spatial distribution of the fractures in this study.

In this study, a discrete fracture network (DFN) model was constructed for the underground powerhouse in the study area solely based on stochastic parameters, as no significant deterministic features such as large faults were identified during the survey. Accuracy is a critical metric for assessing the performance of DFN models, as it directly impacts the feasibility and efficacy of the model in practical applications. In this study, fracture volume density ($P_{32}$) and other parameters were employed as pivotal indicators for model generation. Nevertheless, there may be limitations and potential avenues for future improvement in the model's performance on diverse datasets.

The outcomes of the DFN model underscore the detrimental effect of cracks on the elastoplastic properties of rock masses. A compression deformation test on the rock mass was simulated using PCDC2D, revealing that the vertical deformation modulus is approximately 2 GPa higher than the horizontal modulus. Additionally, the Poisson's ratio is approximately 6% lower in the vertical orientation compared to the horizontal. Analysis of the crack distribution revealed a prevalence of long and large horizontal cracks within the rock mass. In the vertical compression model, most of the cracks intersect with the compressive stress direction at a significant angle, leading to a larger vertical deformation modulus. Conversely, during horizontal compression, most of the cracks intersect with the axial stress direction at a smaller angle (Figs. 13(d–f)), resulting in a smaller horizontal deformation modulus. Under compression, tension and shear cracks concentrate at both ends of the major pre-existing fractures, and these fractures stagger under pressure. Subsequently, new cracks propagate along these pre-existing fracture directions until the rock mass fails completely. The

**Fig. 15** Simulation results obtained using rock classification and DFN model elastic modulus. The first one is the elastic modulus of the intact rock, followed by the DFN model (vertical, horizontal), RQD, RMR + intact rock, and Q-System
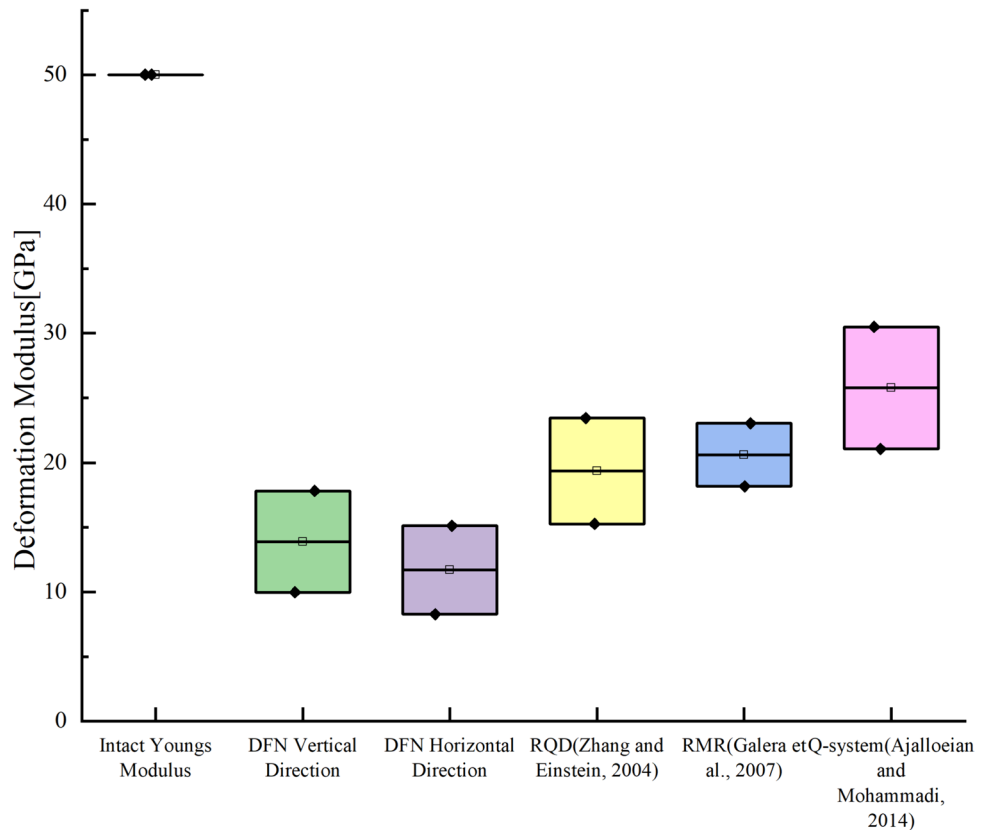
anisotropy of the rock mass is evident due to the axial stress and deviations of the fracture angles within the prefabricated fractures.

The deformation modulus of the rock mass classification method is determined based on the empirical relationships outlined in Table 6, and its discrepancy from the DFN model was evaluated. Notably, the Q-System empirical relationship (Ajalloeian and Mohammadi 2013) yields a higher calculated rock mass deformation modulus compared to other methods. By contrast, the RMR + intact rock method integrates the characteristics of intact rock into the calculation of the rock mass deformation modulus, resulting in more concentrated values compared to those obtained using the DFN model. The DFN model demonstrates high accuracy in capturing the impacts of fractures and faults on the rock mass, particularly in calculating the rock stress field. Additionally, it is essential to account for the variations in rock mechanical parameters resulting from fractures. However, the deformation characteristics of the rock mass under various confining pressures and specific loading conditions necessitate further comprehensive study.

## Conclusions

In this study, a discrete fracture network (DFN) rock mass model was developed based on an on-site adit survey. Uniaxial compression tests were simulated using a hybrid finite-element-discrete-element explicit dynamics numerical computation method. The development of fractures during the compression damage process of the rock mass was analyzed, and the deformation modulus of the rock mass was computed. These results were then compared with those obtained from empirical relationships of traditional engineering rock mass classification schemes.

The presence of numerous fractures within a rock mass plays a pivotal role in the stability analysis of excavations in slope engineering and the underground powerhouses of hydropower stations. Field logging of fractures within an adit was conducted, and a dataset was compiled. Theoretical deductions were made regarding the spatial dimensions, distribution, and bulk density of the fractures. The mechanical properties of the intact rock mass and fractured rock mass were measured in the laboratory, and this data was combined with statistically derived probability density functions and other pertinent information to construct a DFN model that accurately represents the study area.

The modeling results demonstrate that the geometry and mechanical properties of fractures within the rock mass were faithfully represented using the DFN model. The deformation modulus of the fractured rock mass was

observed to decrease significantly by 66% compared to that of the intact rock, while the Poisson's ratio increased by 16%. Furthermore, the modulus derived from compressive deformation exhibited variations of up to 15% across different directions, while the Poisson's ratio varied by 6% depending on the orientation of the fractures. These findings underscore the significant influence of fracture orientation on the mechanical behavior of the rock mass.

By employing rock mass engineering classification schemes (RQD, RMR, and Q-System) and empirical relationships of rock mechanical properties (Zhang and Einstein 2004; Galera et al. 2005; Ajalloeian and Mohammadi 2013), in conjunction with intact rock mechanical parameters, the rock mass quality was assessed in the underground cavern area of the GS power station. The results indicate that, although there are differences between the deformation modulus values obtained using the DFN modeling method and those estimated using the empirical relationships, the former method accounts for the influence of the rock fracture direction on the deformation modulus, highlighting its advantage in addressing rock anisotropy.

The findings of this study, utilizing widely recognized engineering rock mass classification systems and empirical relationships specific to underground caverns, affirm the reliability and accuracy of the DFN modeling method. By calculating the mechanical properties of the rock mass, our approach provides a precise means to capture and describe the anisotropy inherent in rock mechanics research. This enhances our understanding of the mechanical behavior of rock masses and ensures that the resulting data is robust and applicable to practical engineering solutions.

**Authors contribution** Ming Li: Software, Methodology, Data Curation, study, Writing—Original Draft. Hui Deng: Resources, Conceptualization, Supervision. Guoxiang Tu: Writing—Review & Editing.

**Data Availability** Some or all data that support the findings of this study are available from the corresponding author upon reasonable request.

## Declarations

**Competing interest** The authors declare that they have no declaration of competing interest.

## References

Ajalloeian R, Mohammadi M (2013) Estimation of limestone rock mass deformation modulus using empirical equations.

Bull Eng Geol Env 73:541–550. https://doi.org/10.1007/s10064-013-0530-3

Alfano M, Furgiuele F, Leonardi A, Maletta C, Paulino G (2009) Mode I fracture of adhesive joints using tailored cohesive zone models. Int J Fract 157:193–204. https://doi.org/10.1007/s10704-008-9293-4

Andersson J, Shapiro AM, Bear J (1984) A stochastic model of a fractured rock conditioned by measured information. Water Resour Res 20:79–88. https://doi.org/10.1029/WR020i001p00079

Baecher G (1983) Statistical analysis of rock mass fracturing. J Int Assoc Math Geol 15:329–348. https://doi.org/10.1007/BF01036074

Barton N (1978) Suggested methods for the quantitative description of discontinuities in rock masses: International society for rock mechanics. Int J Rock Mech Min Sci Geomech Abstr 15:319–368

Barton N (2002) Some new Q-value correlations to assist in site characterisation and tunnel design. Int J Rock Mech Min Sci 39:185–216. https://doi.org/10.1016/S1365-1609(02)00011-4

Barton N, Lien R, Lunde J (1974) Engineering classification of rock masses for the design of tunnel support. Rock Mech Felsmechanik Mecanique Des Roches 6:189–236. https://doi.org/10.1007/BF01239496

Bieniawski Z (1973) Engineering classification of jointed rock masses. Civil Eng Siviele Ingenieurswese 1973:335–343. https://journals.co.za/doi/pdf/10.10520/AJA10212019_17397. Accessed 7 Aug 2024

Cardona A, Finkbeiner T, Santamarina J (2021) Natural rock fractures: From aperture to fluid flow. Rock Mech Rock Eng 54:1–18. https://doi.org/10.1007/s00603-021-02565-1

Casini G, Hunt DW, Monsen E, Bounaim A (2016) Fracture characterization and modeling from virtual outcrops. AAPG Bull 100:41–61. https://doi.org/10.1306/09141514228

Davy P, Le Goc R, Darcel C (2013) A model of fracture nucleation, growth and arrest, and consequences for fracture density and scaling. J Geophys Res: Solid Earth 118:1393–1407. https://doi.org/10.1002/jgrb.50120

Deere DU (1963) Technical description of rock cores for engineering purpose. Rock Mechanics and Enginee-ring Geology 1:17–22. https://refhub.elsevier.com/S0013-7952(21)00393-8/rf0075

Dershowitz WS, Herda HH (1992) Interpretation of fracture spacing and intensity. p ARMA-92-0757. https://doi.org/10.1016/0148-9062(93)91769-F. Accessed 7 Aug 2024

Dershowitz W, Einstein HH (1988) Characterizing rock joint geometry with joint system models. Rock Mech Rock Eng 21:21–51. https://doi.org/10.1007/BF01019674

Elmo D, Stead D (2009) An integrated numerical modelling-discrete fracture network approach applied to the characterisation of rock mass strength of naturally fractured pillars. Rock Mech Rock Eng 43:3–19. https://doi.org/10.1007/s00603-009-0027-3

Galera JM, Alvarez M, Bieniawski ZT (2005) Evaluation of the deformation modulus of rock masses: comparison of pressuremeter and dilatometer tests with RMR prediction. https://api.semanticscholar.org/CorpusID:110532944. Accessed 7 Aug 2024

Galera MB, Alvarez MAC, Bieniawski ZT, José (2007) Evaluation of the deformation modulus of rock masses using RMR: Comparison with dilatometer tests. In: Workshop on Underground Works under Special Conditions, Madrid, Spain, pp. https://api.semanticscholar.org/CorpusID:133114298. Accessed 7 Aug 2024

González-Fernández MA, Estévez-Ventosa X, Pérez-Rey I, Alejano LR, Masoumi H (2024) Size effects on strength and deformability of artificially jointed hard rock. Int J Rock Mech Min Sci 176:105696. https://doi.org/10.1016/j.ijrmms.2024.105696

Goodman RE (1991) Introduction to rock mechanics. John Wiley & Sons

Gottron D, Henk A (2021) Upscaling of fractured rock mass properties – An example comparing Discrete Fracture Network (DFN) modeling and empirical relations based on engineering rock mass classifications. Eng Geol 294:106382. https://doi.org/10.1016/j.enggeo.2021.106382

Hoek E (1983) Strength of jointed rock masses. Géotechnique 33:187–223. https://doi.org/10.1680/geot.1983.33.3.187

Ivars DM, Davy P, Caroline D, Etienne L, Romain LG, Diane D, Rima G, Sacha E (2021) Rock mechanics and DFN models in the Swedish Nuclear Waste Disposal Program. IOP Conf Ser: Earth Environ Sci 861:042124. https://doi.org/10.1088/1755-1315/861/4/042124

La Pointe PR, Hudson JA (1985) Characterization and Interpretation of rock mass joint patterns. Geolog Soc Am. https://doi.org/10.1130/SPE199

Lavoine E, Davy P, Darcel C, Munier R (2020) A discrete fracture network model with stress-driven nucleation: impact on Clustering, Connectivity, and Topology. Front Phys 8. https://doi.org/10.3389/fphy.2020.00009

Mahabadi OK, Lisjak A, Munjiza A, Grasselli G (2012) Y-Geo: New combined finite-discrete element numerical code for geomechanical applications. Int J Geomech 12:676–688. https://doi.org/10.1061/(ASCE)GM.1943-5622.0000216

Mauldon M, Dunne WM, Rohrbaugh MB (2001) Circular scanlines and circular windows: new tools for characterizing the geometry of fracture traces. J Struct Geol 23:247–258. https://doi.org/10.1016/S0191-8141(00)00094-8

Pahl PJ (1981) Estimating the mean length of discontinuity traces. Int J Rock Mech Min Sci Geomech Abstracts 18:221–228. https://doi.org/10.1016/0148-9062(81)90976-1

Priest SD (1993) Discontinuity analysis for rock engineering. Springer Science & Business Media. https://doi.org/10.1007/978-94-011-1498-1

Priest SD, Hudson JA (1976) Discontinuity spacings in rock. Int J Rock Mech Min Sci Geomech Abstracts 13:135–148. https://doi.org/10.1016/0148-9062(76)90818-4

Read SAL, Perrin ND, Richards L (1999) Applicability of the Hoek-Brown Failure Criterion to New Zealand Greywacke Rocks. https://api.semanticscholar.org/CorpusID:133977497. Accessed 7 Aug 2024

Rohrbaugh MBJ, Dunne WM, Mauldon M (2002) Estimating fracture trace intensity, density, and mean length using circular scan lines and windows. AAPG Bull 86:2089–2104. https://doi.org/10.1306/61EEDE0E-173E-11D7-8645000102C1865D

Schultz RA (1996) Relative scale and the strength and deformability of rock masses. J Struct Geol 18:1139–1149. https://doi.org/10.1016/0191-8141(96)00045-4

Sen Z, Kazi A (1984) Discontinuity spacing and RQD estimates from finite length scanlines. Int J Rock Mech Min Sci Geomech Abstracts 21:203–212. https://doi.org/10.1016/0148-9062(84)90797-6

Sturzenegger M, Stead D (2009) Quantifying discontinuity orientation and persistence on high mountain rock slopes and large landslides using terrestrial remote sensing techniques. Nat Hazard 9:267–287. https://doi.org/10.5194/nhess-9-267-2009

Wang X (2005) Stereological interpretation of rock fracture traces on borehole walls and other cylindrical surfaces. https://api.semanticscholar.org/CorpusID:127918319. Accessed 7 Aug 2024

Wang Y, Zhou X, Wang Y, Shou Y (2018) A 3-D conjugated bond-pair-based peridynamic formulation for initiation and propagation of cracks in brittle solids. Int J Solids Struct 134:89–115. https://doi.org/10.1016/j.ijsolstr.2017.10.022

Wu F, Wang S, Pan B (2022) Statistical mechanics of rock masses(smrm)—inheriting and developing of engineering geomechanics of rock masses. J Eng Geol 30:1–20. https://doi.org/10.13544/j.cnki.jeg.2021-0805

Yao W-W, Zhou X-P, Qian Q-H (2022) From statistical mechanics to nonlocal theory. Acta Mech 233:869–887. https://doi.org/10.1007/s00707-021-03123-0

Zeeb C, Gomez-Rivas E, Bons PD, Blum P (2013) Evaluation of sampling methods for fracture network characterization using outcrops. AAPG Bull 97:1545–1566. https://doi.org/10.1306/02131312042

Zhang L (2016) Determination and applications of rock quality designation (RQD). J Rock Mech Geotech Eng 8:389–397. https://doi.org/10.1016/j.jrmge.2015.11.008

Zhang L, Einstein HH (2000) Estimating the intensity of rock discontinuities. Int J Rock Mech Min Sci 37:819–837. https://doi.org/10.1016/S1365-1609(00)00022-8

Zhang L, Einstein HH (2004) Using RQD to estimate the deformation modulus of rock masses. Int J Rock Mech Min Sci 41:337–341. https://doi.org/10.1016/S1365-1609(03)00100-X

Zhang J-Z, Zhou X-P (2020) Forecasting catastrophic rupture in brittle rocks using precursory ae time series. J Geophys Res: Solid Earth 125:e2019JB019276. https://doi.org/10.1029/2019JB019276

Zhang T, Zhou X-P, Qian Q-H (2023) Drucker-Prager plasticity model in the framework of OSB-PD theory with shear deformation. Engin Comput 39:1395–1414. https://doi.org/10.1007/s00366-021-01527-z

Zhang T, Gu T, Jiang J, Zhang J, Zhou X (2024) An ordinary state-based peridynamic model for granular fracture in polycrystalline materials with arbitrary orientations in cubic crystals. Eng Fract Mech 301:110023. https://doi.org/10.1016/j.engfracmech.2024.110023

Zheng Z, Deng B, Liu H, Wang W, Huang S, Li S (2024a) Microdynamic mechanical properties and fracture evolution mechanism of monzogabbro with a true triaxial multilevel disturbance method. Int J Min Sci Technol 34:385–411. https://doi.org/10.1016/j.ijmst.2024.01.001

Zheng Z, Xu H, Zhang K, Feng G, Zhang Q, Zhao Y (2024b) Intermittent disturbance mechanical behavior and fractional deterioration mechanical model of rock under complex true triaxial stress paths. Int J Min Sci Technol 34:117–136. https://doi.org/10.1016/j.ijmst.2023.11.007

Zhou XP, Bi J, Qian QH (2015) Numerical simulation of crack growth and coalescence in rock-like materials containing multiple pre-existing flaws. Rock Mech Rock Eng 48:1097–1114. https://doi.org/10.1007/s00603-014-0627-4

Zhou X-P, Zhang J-Z, Qian Q-H, Niu Y (2019) Experimental study of progressive cracking processes in granite under uniaxial loading using digital imaging and AE techniques. J Struct Geol 126:129–145. https://doi.org/10.1016/j.jsg.2019.06.003

Zhou X, Yao W-W, Berto F (2021) Smoothed peridynamics for the extremely large deformation and cracking problems: Unification of peridynamics and smoothed particle hydrodynamics. Fatigue Fract Eng Mater Struct 44:2444–2461. https://doi.org/10.1111/ffe.13523